nature materials

SUPPLEMENTARY INFORMATION

DOI: 10.1038/NMAT4356

# Resonant internal quantum transitions and femtosecond radiative decay of excitons in monolayer $WSe_2$

C. Poellmann[1], P. Steinleitner[1], U. Leierseder[1], P. Nagler[1], G. Plechinger[1], M. Porer[1], R. Bratschitsch[2], C. Schüller[1], T. Korn[1], and R. Huber[1]

[1] *Department of Physics, University of Regensburg, D-93040 Regensburg, Germany*

[2] *Institute of Physics, University of Münster, D-48149 Münster, Germany*

## Table of contents

DOI: 10.1038/NMAT4356

## 1. Interband and intra-excitonic absorption

As discussed in the main text, optically bright excitons in a semiconductor can be created (annihilated) by absorption (emission) of a photon of resonant energy ħω. For Wannier excitons, the absorption coefficient for one-photon interband transitions fulfills the following relation[1]

$$\alpha_{IB}(\omega) \sim |d_{cv}|^2 \sum_{\mu} \left|\psi_{\mu}(\vec{r}=0)\right|^2 \quad (1)$$

Here $d_{cv}$ is the interband dipole matrix element evaluated with single-electron Bloch waves in the conduction and valence bands. $\psi_{\mu}(\vec{r}=0)$ marks the slowly varying envelope function of the excitons, characterized by the quantum number μ. Importantly, the envelope function is evaluated at vanishing distance $\vec{r}$ between electron and hole. Furthermore, momentum conservation in combination with the small momentum of a photon in the visible spectral range stipulates that optical absorption creates excitons with vanishing centre-of-mass momentum $K$.

In contrast, intra-excitonic absorption of a gas of Wannier excitons in the 1s quantum state is found by analogy with quantum transitions in the hydrogen atom to scale as

$$\alpha_{IE}(\omega) \sim \sum_{\mu} \left|\langle \psi_{\mu} | \vec{r} | \psi_{1s} \rangle\right|^2 \quad (2)$$

Note that the intra-exitonic absorption depends on the full spatial profile of the exciton's envelope functions, but is independent of the interband dipole moment $d_{cv}$, which is typically a complicated quantity to compute. Furthermore, mid-infrared radiation can couple to the orbital degree of freedom of all 1s excitons, irrespectively of $K$, since this process does not create or annihilate excitons, but it probes a pre-existing ensemble of electron-hole pairs. Measurements of the internal Rydberg-like mid-infrared absorption of excitons are, therefore, the most direct way of retrieving quantitative information on the internal structure, envelope functions, oscillator strengths, densities and dynamics of all excitons with arbitrary momentum $K$.

## 2. Interband absorbance of monolayer $WSe_2$

Supplementary Fig. 1 displays the measured linear absorption spectrum (red solid curve) of the $WSe_2$ monolayer characterized in Fig. 1 of the main text. By calculating the overlap integral with the pump spectrum (blue broken curve), the number of absorbed pump photons $n_a$ can be determined from the total pump fluence. In the main paper, the value retrieved in this way (Fig. 3a, dashed line) is compared with the density of resonantly injected excitons $n_X$ (Fig. 3a, red spheres).

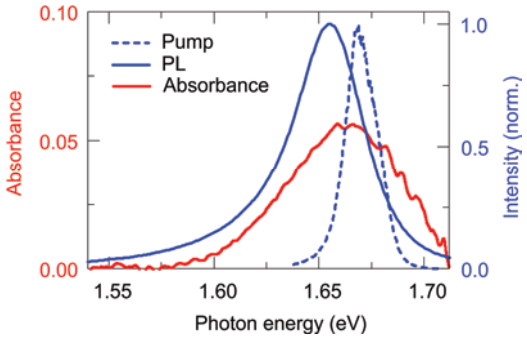


**Supplementary Figure 1 | Spectral absorbance.** Spectral absorbance (red line) and PL intensity (blue solid line) of the $WSe_2$ monolayer depicted in Figs. 1b and c, together with the pump spectrum (blue dashed line) used in the experiments underlying Figs. 1-4.

### 3. Mid-infrared response of photoexcited bulk $WSe_2$

It is instructive to compare the photo-induced mid-infrared response of monolayer $WSe_2$ (Figs. 1e and 2) with data taken in a bulk $WSe_2$ crystal under identical experimental conditions (Supplementary Fig. 2). Utilizing atomic force microscopy, the thickness of the specimen is determined as 20 nm. In the bulk sample, optical pumping with a spectrum shown in Fig. 1d (pump fluence $\Phi = 42\ \mu J/cm^2$) creates unbound electron-hole pairs far above the indirect bandgap of the material ($E_{g,bulk} = 1.2$ eV). $\Delta E(t_{EOS})$ recorded at $t_{pp} = 75$ fs (red curve) exhibits a phase shift of $\pi/2$ (Supplementary Fig. 2a), in stark contrast to the response of the monolayer (Fig. 1e) where the phase between $\Delta E$ and $E_{ref}$ is shifted by $\pi$. For the bulk case (Supplementary Fig. 2a), the maxima, thus, occur at the zero-crossings of the reference electric field, indicating an effective temporal shift of the probe transient towards earlier times. This response is typical of a Drude gas of unbound electron-hole pairs that modifies the effective optical path length through the sample. Indeed the spectra of the real parts of the optical conductivity $\Delta\sigma_1$ (Supplementary Fig. 2b) and the dielectric function $\Delta\varepsilon_1$ (Supplementary Fig. 2c), confirm that the response is mostly inductive, i.e. dominated by $\Delta\varepsilon_1$, whereas the photo-induced conductivity change is reduced by almost one order of magnitude with respect to the situation in the monolayer sample. Furthermore, no resonance is seen in Supplementary Fig. 2.

A Drude model (black dashed lines) reproduces $\Delta\varepsilon_1(\omega)$ fairly well and coarsely accounts for $\Delta\sigma_1$. For optimal fits, we extract a scattering time of 42 fs and a density of free carriers of $4.3 \times 10^{19}$ $cm^{-3}$, in good agreement with the density of absorbed photons.

DOI: 10.1038/NMAT4356

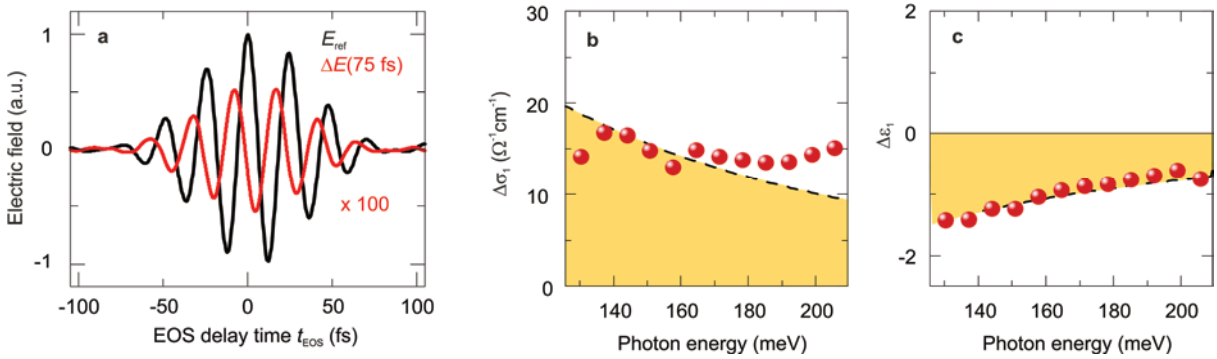


**Supplementary Figure 2 | Drude response of bulk $WSe_2$. a,** Waveform of the probe pulse $E_{ref}$ (black) transmitted through the unexcited $WSe_2$ monolayer and pump-induced change $\Delta E$ (red, scaled up by a factor of 100) at $t_{pp} = 75$ fs after pumping of a photoexcited 20 nm thick bulk $WSe_2$ with an 90-fs pulse featuring the spectrum depicted in Fig. 1d (pump fluence, $\Phi = 42\ \mu J/cm^2$). **b,** Corresponding real part of the pump-induced mid-infrared conductivity $\Delta\sigma_1(\hbar\omega)$ as a function of photon energy, $\hbar\omega$. **c**, Corresponding real part of the dielectric function, $\Delta\varepsilon_1(\hbar\omega)$. Red spheres: Experimental data; black dashed curve: Drude model simultaneously fitting $\Delta\sigma_1$ and $\Delta\varepsilon_1$. The adapted parameters for the carrier density and the Drude scattering time are $4.3 \times 10^{19}$ cm$^{-3}$ and 42 fs, respectively.

## 4. Pump wavelength dependence of the dielectric response of monolayer $WSe_2$

Supplementary Figure 3 summarizes the mid-infrared response of the photoexcited monolayer of $WSe_2$ for various pump wavelengths. All data are taken at room temperature. Upon non-resonant above-bandgap excitation (pump wavelength: 400 nm; FWHM: 10 nm; Supplementary Fig. 3a), $\Delta\sigma_1$ (Supplementary Fig. 3b) and $\Delta\varepsilon_1$ (Supplementary Fig. 3c) exhibit spectral shapes that are characteristic of unbound electron-hole pairs. A Drude model reproduces the experimental response functions reasonably well (Supplementary Figs. 3b,c, black dashed curves).

The second column in Supplementary Fig. 3 (panels d-f), reports measurements performed with a pump spectrum centred at 742 nm, i.e. at the high-energy wing of the interband 1s exciton resonance (Supplementary Fig. 3d). This excitation scenario is identical to the one discussed in Figs. 1-4 of the main manuscript. The spectral response functions, $\Delta\sigma_1$ and $\Delta\varepsilon_1$, recorded at a pump delay time of $t_{PP} =$ 275 fs, are characteristic of the excitonic 1s-2p transition (Supplementary Figs. 3e,f).

Both $\Delta\sigma_1$ and $\Delta\varepsilon_1$ can be simultaneously fit by the two-dimensional Wannier exciton model (Supplementary Eq. 14), assuming realistic values of the exciton density (Supplementary Figs. 3e,f, dashed curves). The extracted parameters for the two-dimensional Wannier exciton model are given in the figure caption.

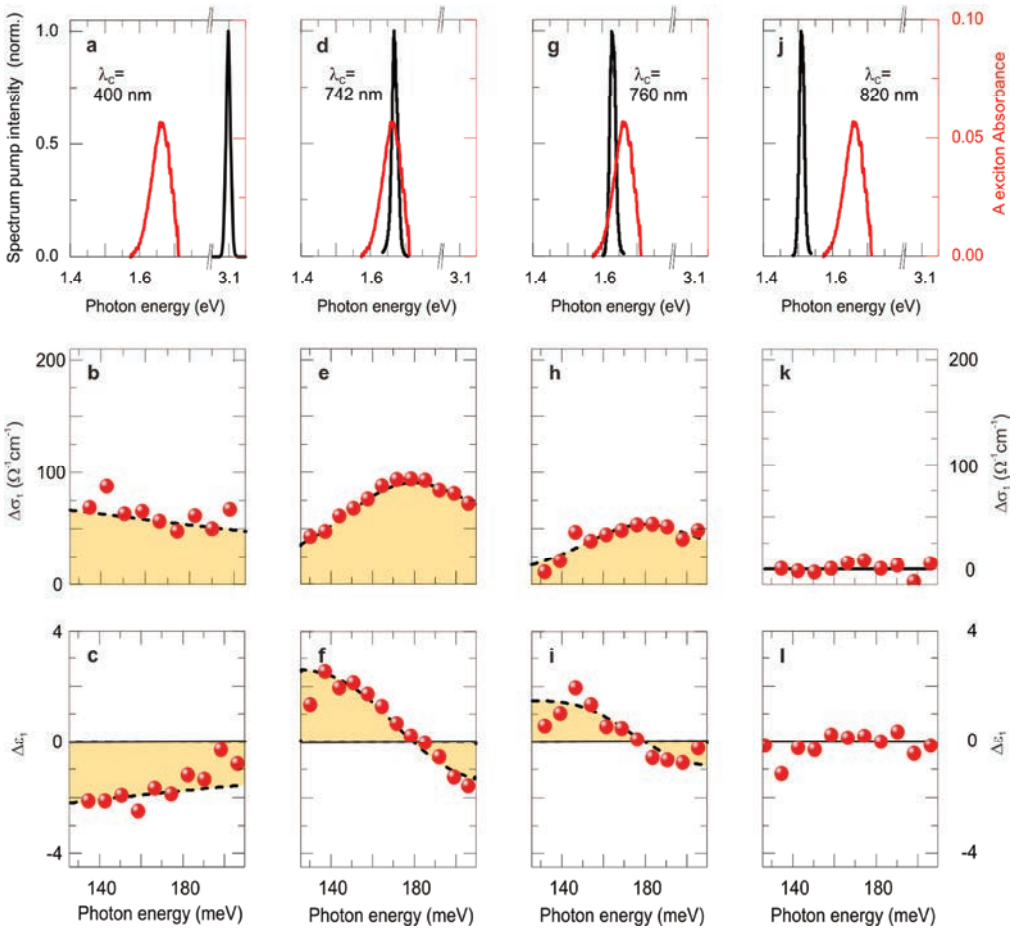


**Supplementary Figure 3 | Mid-infrared response of photoexcited monolayer $WSe_2$ for various pump wavelengths at $T$ = 295 K.** **a** – **c**, Data collected with a pump centred at $\lambda_C$ = 400 nm. **a**, Pump spectrum (black solid curve) and spectral absorbance of the 1s A exciton (red solid line). **b, c**, $\Delta\sigma_1(\hbar\omega)$ and $\Delta\varepsilon_1(\hbar\omega)$ at $t_{PP}$ = 500 fs. Red spheres: experiment. Black dashed curves: Drude model with an electron-hole pair density of $1.4 \times 10^{12}$ cm$^{-2}$ and a scattering time of 18 fs. **d** – **f**, Analogous data collected for a pump spectrum centred at $\lambda_C$ = 742 nm (**d**). **e, f,** $\Delta\sigma_1(\hbar\omega)$ and $\Delta\varepsilon_1(\hbar\omega)$ at $t_{PP}$ = 275 fs. Red spheres: experiment. Black dashed curves: numerical fit via 2D exciton model ($n_X = 1.8 \times 10^{12}$ cm$^{-2}$, $E_{res}$ = 179 meV, $\Delta$ = 105 meV). **g** – **i**, Analogous data for a pump spectrum (**g**) centred at $\lambda_C$ = 760 nm. **h, i,** $\Delta\sigma_1(\hbar\omega)$ and $\Delta\varepsilon_1(\hbar\omega)$ at $t_{PP}$ = 275 fs. Red spheres: experiment. Black dashed curves: numerical fit via 2D exciton model ($n_X = 1.1 \times 10^{12}$ cm$^{-2}$, $E_{res}$ = 179 meV, $\Delta$ = 90 meV. **j** – **l**, For a pump spectrum centred at $\lambda_C$ = 820 nm (**j**), no measurable mid-infrared response is observed (**k, l**).

The third column of Supplementary Fig. 3 repeats the experiments with a slightly longer pump wavelength of 760 nm, corresponding to excitation at the low-energy wing of the 1s exciton line (Supplementary Fig. 3g). The spectral response functions $\Delta\sigma_1$ and $\Delta\varepsilon_1$ (Supplementary Figs. 3h,i) are very similar to the case shown in Supplementary Figs. 3e,f. Importantly, we find the same energy of the 1s-2p resonance (179 meV), which confirms the microscopic picture of the intrinsic properties of excitons being responsible for the resonance (1s-2p transition).

DOI: 10.1038/NMAT4356

Finally, exciting the monolayer with a pump centred at 820 nm (last column of Supplementary Fig. 3) does not lead to any measurable absorption, since the pump-wavelength is energetically far below the 1s excitonic interband resonance of 744 nm (Supplementary Fig. 3j). Accordingly the spectral response functions $\Delta\sigma_1$ and $\Delta\varepsilon_1$ for a pump delay time of $t_{PP}$ = 275 fs vanish (Supplementary Figs. 3k,l).

**5. Two-dimensional Wannier exciton model for monolayer $WSe_2$**

We model the properties of the observed A excitons in $WSe_2$ using the slowly-varying envelope approximation of two-dimensional Wannier excitons. In this framework, the total exciton wave function is composed of a wavepacket of Bloch functions from the conduction and valence bands. The relative motion of electron and hole is captured by an envelope function which is obtained in formal analogy with the two-dimensional hydrogen atom, scaled by the reduced effective band mass μ and modified by dielectric screening. The stationary Schrödinger equation for the envelope functions ψ in polar coordinates $r$ and φ is given by

$$\left[-\frac{\hbar^2}{2\mu}\left(\frac{\partial^2}{\partial r^2}+\frac{1}{r}\frac{\partial}{\partial r}+\frac{1}{r^2}\frac{\partial^2}{\partial \varphi^2}\right)+V_{\mathrm{eh}}(r)\right]\psi(r,\varphi)=E\psi(r,\varphi) \tag{3}$$

where $V_{\mathrm{eh}}(r)$ is the interaction potential. Note that in this equation we have only taken into account the relative motion of electron and hole described by their distance $r$. The centre-of-mass motion is trivially described with a plane wave with momentum $K$.

Separating the variables via $$\psi(r,\varphi)=R(r)\Phi(\varphi) \tag{4}$$

one obtains $$\Phi(\varphi)=\frac{1}{\sqrt{2\pi}}e^{il\varphi} \tag{5}$$

with the quantum number $$l=0,\pm1,\pm2,\ldots \tag{6}$$

describing the angular momentum. The radial part $R(r)$ of the wavefunction solves the equation

$$\frac{\partial^2}{\partial r^2}R(r)+\frac{1}{r}\frac{\partial}{\partial r}R(r)+\left\{\frac{2\mu}{\hbar^2}[E-V_{\mathrm{eh}}(r)]-\frac{l^2}{r^2}\right\}R(r)=0 \tag{7}$$

The quantum number $l=0$ corresponds to s-states, $l=\pm1$ to p-states and so on.

The ansatz $$R(r)=r^{-1/2}u(r) \tag{8}$$

leads to the 1D Schrödinger equation

$$\left[-\frac{\hbar^2}{2\mu}\frac{\partial^2}{\partial r^2}+V_{\mathrm{eff}}(r)\right]u(r)=Eu(r) \tag{9}$$

with an effective potential

$$V_{\mathrm{eff}}(r) = V_{\mathrm{eh}}(r) + \frac{\hbar^2}{2\mu r^2}(l^2 - 1/4) \tag{10}$$

In the simplest case the interaction potential $V_{\mathrm{eh}}(r)$ can be described with a locally screened Coulomb interaction potential (cgs-units) given by

$$V_{\mathrm{eh}}(r) = -\frac{e^2}{\varepsilon r} \tag{11}$$

where ε is the dielectric constant of the monolayer (ε = 4.5, see Ref. 2). For this potential, an analytic solution can be found (simple 2D hydrogen model[3]).

Following the theory of Refs. 4 and 5, however, a correct description of the physics of a monolayer system calls for nonlocal screening due to a non-uniform dielectric environment. The interaction potential is then given by (cgs-units)

$$V_{\mathrm{eh}}(r) = -\frac{\pi e^2}{2r_0}\left[H_0\left(\frac{(1+\varepsilon_s)r}{2r_0}\right) - Y_0\left(\frac{(1+\varepsilon_s)r}{2r_0}\right)\right] \tag{12}$$

with the dielectric constant of the substrate, $\varepsilon_s$, and the screening length in the absence of a substrate, $r_0$. Furthermore, $H_0$ is the Struve function of order 0. $Y_0$ represents the Neumann function of order 0. The potential is proportional to the simple Coulomb interaction $\propto \frac{1}{r}$ for large $r$, but proportional to $\log(r)$ for small separation. In contrast to the interaction potential for the simple 2D hydrogen model, this nonlocally-screened interaction potential can only be treated numerically. Both potentials are shown in Fig. 2h.

By numerically solving the 1D Schrödinger equation (Supplementary Equation 9) with the nonlocally screened interaction potential one obtains the radial distribution function $rR^2_{1s,2p}$ as shown in Fig. 2g as well as the eigenenergies $E_{1s,2p}$ as shown in Fig. 2h. The dielectric constant of the CVD diamond substrate is assumed to be $\varepsilon_s = 5.64$ and the screening length $r_0$ is chosen such that the transition energy $|E_{1s} - E_{2p}|$ matches our experimentally determined value of 170 meV. The screening length turns out to be $r_0 = 27$ Å. According to Ref. 6, $r_0$ can be calculated by $r_0 = \frac{\varepsilon_2^2 - 1}{2\varepsilon_2} d_{\mathrm{eff}}$, where $\varepsilon_2 = \sqrt{\varepsilon_\perp \varepsilon_\parallel}$ and the effective layer thickness $d_{\mathrm{eff}} = d \cdot \sqrt{\varepsilon_\parallel/\varepsilon_\perp}$. $\varepsilon_\perp$ and $\varepsilon_\parallel$ are the components of the static dielectric tensor of *bulk* $WSe_2$. With $\varepsilon_\perp = 11.7$ and $\varepsilon_\parallel = 8.7$ and $d = 7$ Å for $WSe_2$[2] one finds $r_0 = 30$ Å, which is in good agreement with our value.

The excitonic 1s-2p intraband oscillator strength including the degeneracy of the 2p-state ($l = \pm 1$) is given in Ref. 7:

$$f_{1s-2p} = \frac{2\mu}{\hbar^2}|E_{1s} - E_{2p}|\left|\langle\psi_{2p}|\hat{x}|\psi_{1s}\rangle\right|^2 \tag{13}$$

DOI: 10.1038/NMAT4356

We find $f_{1s-2p} = 0.32$ using the numerically determined wavefunctions $\psi_{1s,2p} = R_{1s,2p} \times \Phi_{1s,2p}$, $\mu = 0.167 \times m_0$, and $|E_{1s} - E_{2p}| = 170$ meV.

In order to reproduce both real and imaginary part of the experimentally extracted dielectric function with the theoretical Wannier exciton model, we finally introduce phenomenological broadening. This is achieved by modelling the 1s-2p transition as a Lorentzian oscillator:

$$\Delta\varepsilon(\omega) = \frac{n_X e^2}{\varepsilon_0 \mu} \times \frac{f_{1s-2p}}{\frac{E_{res}^2}{\hbar^2} - \omega^2 - i\omega\Delta} \qquad (14)$$

with the fit parameters exciton density $n_X$, resonance frequency $E_{res}$ and linewidth $\Delta$.

## 6. Comparison of the 1s-2p transition energy extracted from intra- and interband spectroscopy

The energy of the 1s-2p transition of the A exciton found in the experiments is compatible with literature values measured by interband spectroscopy under different conditions. In the work of He et al.[8] the 1s-2p transition amounts to roughly 225 meV with an uncertainty of about 30%. The more recent work by Wang et al.[9] reports a level spacing between the 1s and the 2p states of 140 meV. This energy is slightly different from the energy of 170 meV which we measured directly by means of THz spectroscopy of the intra-excitonic transition. This discrepancy may be explained by the different effective screening of the excitonic binding potential due to the different substrates used in the experiments (for the influence of the substrate see Ref. 5). While our sample is placed on a CVD diamond substrate, Wang et al.[9] employ a $SiO_2$ substrate. Furthermore, surface adatoms may influence the level spacing, too.

## 7. The role of trions

The mid-infrared response of the photoexcited single-layer $WSe_2$ sample investigated in the main text is dominated by neutral excitons. Even though the subtle fine structure observed in $\Delta\sigma_1$ and $\Delta\varepsilon_1$ at delay times $t_{PP} > 1$ ps (Fig. 2 e, f) may be an indication of trionic correlations, their influence is relatively weak for the following reasons:

1. The optical pump pulses are spectrally located at the high-energy wing of the interband resonance of the 1s A exciton (see Fig. 1d). For an estimated binding energy of about 30 meV[10], trions are not expected to be directly generated by optical injection. Scattering processes are required to dissipate the

excess energy. Yet such processes are efficient only at low temperatures, which leads to the second argument:

2. The experiments take place at room temperature, whereas the experiments from Refs. 10 - 12 have been performed at low temperature. In a temperature scan, Wang et al.[11] observe the disappearance of the trion PL line above 200 K due to thermal dissociation.

3. The density of background doping is relatively low in the $WSe_2$ sample used here. This point is confirmed by comparing the PL intensity of excitons and trions in $WSe_2$. Supplementary Figs. 4a and b compare the PL intensity from monolayers of $WSe_2$ (from the same batch used in the manuscript) and a $MoSe_2$ reference. At low temperatures, the trion peak is much weaker in $WSe_2$ as compared to $MoSe_2$ under similar excitation conditions; at room temperature the trion peak is not discernible in either compound. In addition, the trion line of the $WSe_2$ monolayer flake is even substantially weaker than the one shown in Fig. 1(c) of Ref. 11, suggesting relatively low background doping in our $WSe_2$ flakes. Based on the work by Fang et al.[13] it is expected that the background doping density in $WSe_2$ flakes used here is below $10^{11}$ $cm^{-2}$. This number is more than one order of magnitude smaller than the density of optically injected neutral excitons in the experiments. Even at low temperature, only a minor fraction of excitons could, thus, form trions for numerical reasons.

4. The spectral response of the photoexcited sample is quantitatively described by the 1s-2p transition of neutral excitons. Since the same model needs to reproduce both $\Delta\sigma_1$ and $\Delta\varepsilon_1$, simultaneously, this is a quite stringent benchmark for realistic models. The fine structure of trions is expected to be more complex – somewhat similar to the hydrogen anion. As mentioned in the main text, the subtle fine structure in Figs. 2e and f might be a first indication of trions, but the spectral weight is too weak yet to draw clear conclusions as to the structure and dynamics of trions.

5. Finally, the dynamics observed in the experiments is perfectly reconcilable with time resolved PL as e.g. in Refs. 11 and 14 in a picture of neutral excitons, whereas trions have been shown to follow a substantially slower decay dynamics.

DOI: 10.1038/NMAT4356

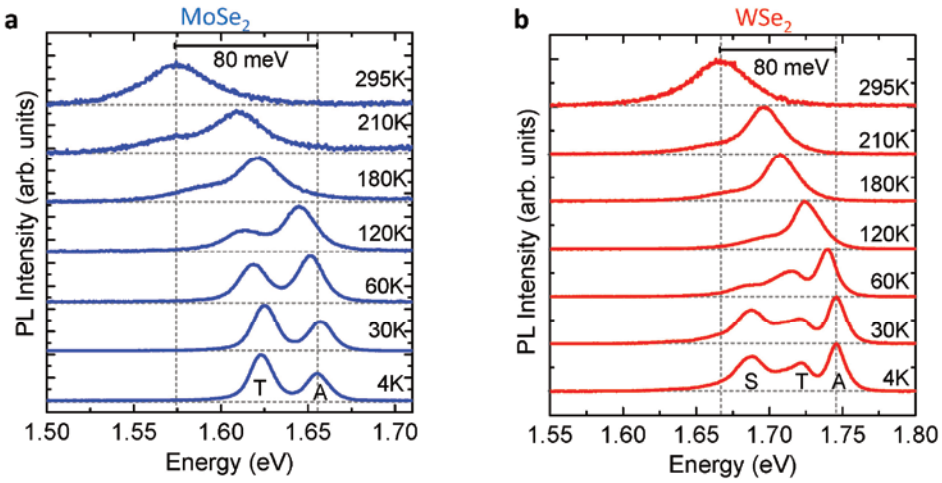


**Supplementary Figure 4 | Interband photoluminenscence spectra of monolayer $MoSe_2$ and $WSe_2$. a**, PL spectra of monolayer $MoSe_2$ for different lattice temperatures. **b**, Corresponding data from monolayer $WSe_2$ taken from the same bulk crystal source used in the manuscript. The spectral positions of the 1s A excitons (A), the trions (T) and localized exciton states (S) are indicated. With increasing temperature, the exciton lines redshift (in agreement with the Varshni formula) and broaden and the relative weight of trions decreases. Since PL is the time-integrated result of multi-scale dynamics involving photogeneration, momentum- and energy scattering, formation of trions (at low temperatures) and radiative recombination, PL will be more sensitive to low-energy states, such as trions, than higher-energy states, such as 1s excitons. Still the trion intensity is much weaker than the free-exciton peak. This provides evidence that even on extended timescales the density of neutral excitons strongly exceeds the density of trions in the $WSe_2$ sample.

### 8. Density dependence of intra-excitonic resonance

Figure 3 in the main text summarizes the dependence of $n_X$, $E_{res}$ and $\Delta$ on the pump fluence $\Phi$. These data are extracted by fitting the two-dimensional exciton model to the dielectric response functions measured for five different fluences, at a fixed delay time $t_{PP}$ = 75 fs (Supplementary Fig. 5).

### 9. Linewidth of the 1s-2p transition and its dynamics

The linewidth of the 1s-2p resonance is likely dominated by the broadening of the 2p state. Even though the exciton density is still below the Mott density estimated by close packing of 1s excitons, this statement is not true for the more extended 2p state. The combination of a relatively large Bohr radius (~ 3 nm) and the high excitation density required in the experiment cause sizable overlap between neighbouring excitons. In this situation exciton-exciton scattering could be efficient for 2p states.

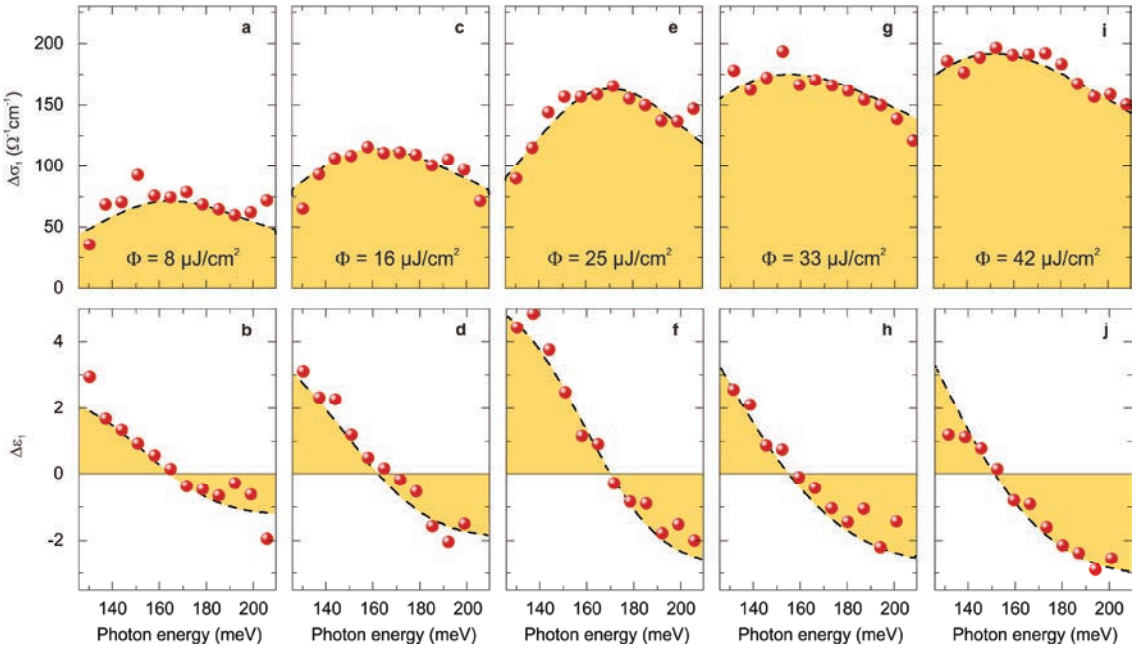


**Supplementary Figure 5 | Density dependent dielectric response. a**, **c**, **e**, **g**, **i**, Real part of the pump-induced mid-infrared conductivity $\Delta\sigma_1(\hbar\omega)$ of a photoexcited monolayer $WSe_2$, as a function of photon energy, $\hbar\omega$, for five different pump fluences $\Phi$ at a fixed pump delay time $t_{PP}$ = 75 fs. **b**, **d**, **f**, **h**, **j**, Corresponding real part of the dielectric function, $\Delta\varepsilon_1(\hbar\omega)$. Red spheres: Experimental data; black dashed curve: Two-dimensional Wannier exciton model simultaneously fitting $\Delta\sigma_1$ and $\Delta\varepsilon_1$. The adapted parameters of exciton density $n_X$, transition energy $E_{res}$ and linewidth $\Delta$ are given in Fig. 3.

In fact, Supplementary Fig. 6 shows that the width of the 1s-2p resonance decreases strongly at lower excitation densities. Extrapolating the measured data at $t_{PP}$ = 75 fs of Supplementary Fig. 6 towards zero density with a least-square linear fit provides an intrinsic width of the resonance of 90 meV. Given a width of the 1s resonance of 45 meV and assuming a slightly wider 2p resonance would account for the experimental finding reasonably well. Since 2p excitons are energetically degenerate with large-momentum 1s states (Fig. 1a) there is a large phase space for scattering of 2p excitons and it is reasonable to expect stronger broadening of the 2p vs. the 1s state. Phonon scattering likely plays a key role in the broadening of the 2p state (see also discussion of Supplementary Fig. 9).

On a more subtle level, the ultrashort radiative decay broadens optically bright 1s states by 9 meV, contributing to the PL linewidth. This broadening should also add to the 1s-2p linewidth $\Delta$, yet only for $K \approx 0$. Although $\Delta$ is always dominated by the width of the 2p state, the 1s-2p resonance of a bright exciton ensemble at $t_{PP}$ = 75 fs (Supplementary Fig. 6, red spheres) is indeed tentatively broader than the corresponding resonance at $t_{PP}$ = 0.8 ps and 1.6 ps, when the excitons are mostly dark (Supplementary Fig. 6, black triangles).

DOI: 10.1038/NMAT4356

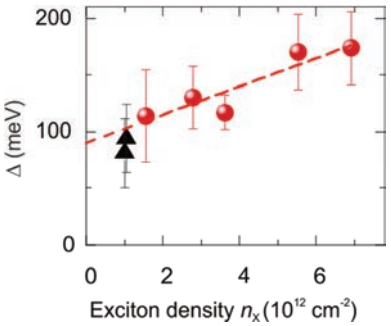


**Supplementary Figure 6 | Exciton linewidth Δ as a function of density $n_X$.** Red spheres: Data extracted by fitting the mid-infrared response functions for $t_{PP}$ = 75 fs, as in Fig. 3c. Black triangles: Linewidths obtained for delay times $t_{PP}$ = 0.8 ps and 1.6 ps. Dashed red line: Least-square linear fit to the data at $t_{PP}$ = 75 fs (red spheres).

## 10. Field-resolved optical pump/mid-infrared probe spectroscopy

In order to map out the dynamics of the full dielectric response of the photoexcited $WSe_2$ monolayer we employ optical pump/mid-infrared probe spectroscopy with field-resolving detection of the probe waveform. The schematic is shown in Supplementary Fig. 7.

An optical pump selectively injects 1s excitons. After a variable delay time $t_{PP}$ a phase stable mid-infrared probe pulse propagates through the sample. The waveform transmitted through the sample is focused onto a thin electro-optic crystal. A co-propagating 12-fs near-infrared gate pulse samples the momentary birefringence induced by the transient carrier wave of the probe pulse. By a systematic variation of the delay time $t_{EOS}$ between the probe transient and the gate a complete image of the oscillating carrier wave of the mid-infrared field transient is obtained. The waveform transmitted through the excited and the unexcited sample is directly compared to obtain $E_{ref}$ and $\Delta E$ as discussed in the main text (Fig. 1e). By Fourier transformation of the time-domain data of $\Delta E(t_{EOS})$ and $E_{ref}(t_{EOS})$ and standard Fresnel analysis[15], the complete complex-valued dielectric function or, alternatively, $\Delta\sigma_1$ and $\Delta\varepsilon_1$ can be extracted as shown in Fig. 2 and Supplementary Figs. 3, 5.

For a nearly bandwidth limited mid-infrared pulse used in the experiment, one can show that the maximum pump-induced change of the transmitted electric field $\Delta E_{max}$ is directly proportional to the spectrally integrated response of the system. This fact can be seen as follows (see also Refs. 16 and 17).

The frequency domain data of the complex-valued pump induced change, $\Delta E$, can be expressed as a product of a real-valued amplitude $\Delta\mathcal{E}(\omega)$ and an exponential function containing the phase $\varphi$:

$$\Delta E(\omega) = \Delta\mathcal{E}(\omega)\exp\left(-i\varphi(\omega)\right) \tag{15}$$

Fourier transformation takes $\Delta E$ back into the time domain:

$$\Delta E(t_{\mathrm{EOS}}) \propto \int_{-\infty}^{+\infty} \Delta\mathcal{E}(\omega) \exp\left(-i\varphi(\omega)\right) \cdot \exp(i\omega t_{\mathrm{EOS}})\, d\omega \tag{16}$$

For a nearly bandwidth limited (almost unchirped) pulse the frequency dependence of the phase is nearly linear $\varphi(\omega) = \varphi_0 + t_0 \cdot \omega$. Here $t_0$ represents the maximum of $\Delta E$ in the time domain. Thus $\Delta E$ can be rewritten as

$$\Delta E(t_{\mathrm{EOS}}) \propto \int_{-\infty}^{+\infty} \Delta\mathcal{E}(\omega) \cdot \exp(i\omega\,(t_{\mathrm{EOS}} - t_0))\, d\omega \tag{17}$$

The maximum of the modulus of $\Delta E(t_{\mathrm{EOS}})$ is reached when $t_{\mathrm{EOS}} = t_0$. In this case Eq. (17) simplifies as

$$\Delta E_{\max} = \Delta E(t_{\mathrm{EOS}} = t_0) \propto \int_{-\infty}^{+\infty} \Delta\mathcal{E}(\omega)\, d\omega \tag{18}$$

Thus, the maximum amplitude of the pump induced field change is proportional to the spectrally integrated response of the system. Since the changes in the transmission $\Delta E(\omega)$ are exclusively caused by the 1s-2p excitonic resonance (see Fig. 2), the maximum of the pump induced change, $\Delta E_{\max}$, can directly be attributed to the spectrally integrated change of the dielectric function, $\int_{-\infty}^{+\infty} \Delta\varepsilon(\omega)\, d\omega$. The latter scales linearly with the exciton density $n_{\mathrm{X}}$. Instead of acquiring the full two dimensional dataset as a function of $t_{\mathrm{PP}}$ and $t_{\mathrm{EOS}}$, the time dynamics of the exciton density can be deduced from a 1D scan of $\Delta E_{\max}$:

$$n_{\mathrm{X}}(t_{\mathrm{PP}}) \propto \Delta E_{\max}(t_{\mathrm{PP}}) \tag{19}$$

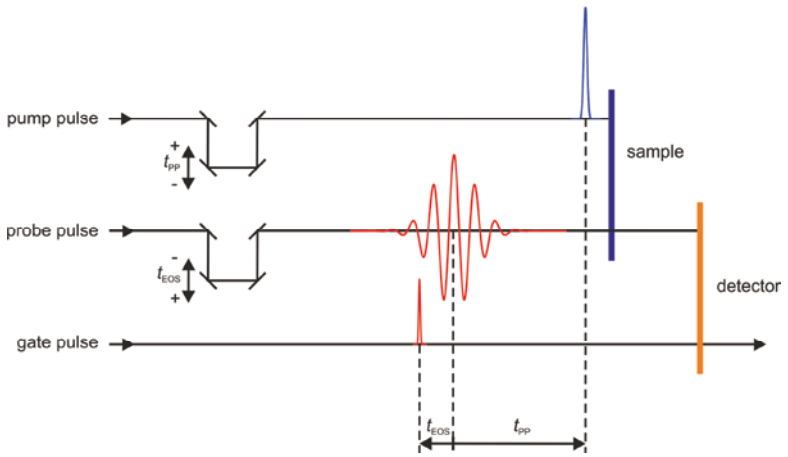


**Supplementary Figure 7 | Two-time dependent pump-probe spectroscopy.** A pump pulse induces a change in the dielectric function of a sample. After the time interval $t_{\mathrm{PP}}$ a mid-infrared field transient probes the system. Its waveform is scanned via a gate pulse that copropagates through the detector crystal with a variable delay time

DOI: 10.1038/NMAT4356

### 11. Rate equation model for exciton dynamics and quantum yield

The time dynamics of the exciton density $n_X$ can be modeled with a set of rate equations taking into account all relevant generation and decay mechanisms of all excitons. We distinguish between two subsets of excitons – optically dark large-momentum states and optically bright states featuring momenta within the light cone, as illustrated in Supplementary Fig. 8a.

The density of bright excitons, which decay radiatively, is denoted by $n_{RX}$, whereas non-radiative dark

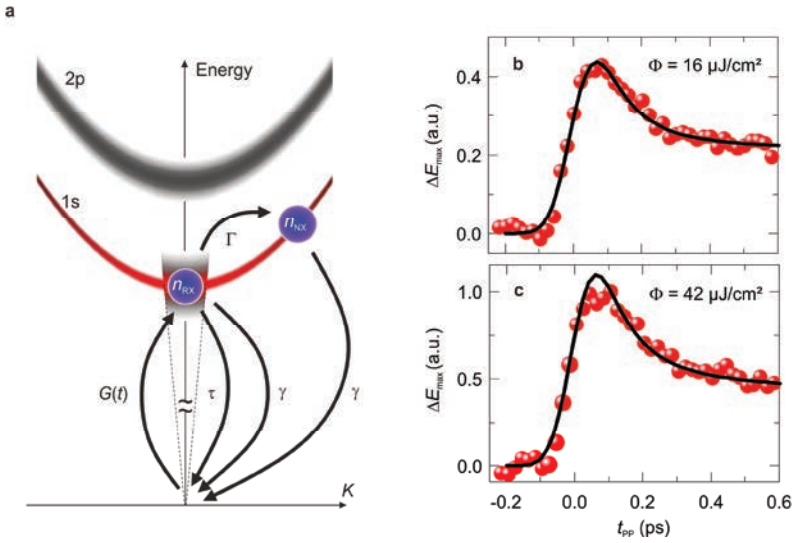


**Supplementary Figure 8 | Rate equation model. a,** Schematic exciton dispersion and separation of excitons into a subset of optically bright 1s states (density $n_{RX}$) featuring small $K$ vectors within the light cone (dashed line) and non-radiative states (density $n_{NX}$) at large $K$ vectors remaining dark for interband transitions. $G(t)$ describes the generation rate by pump-induced interband transitions, $\tau$ is the time constant for radiative recombination. $\Gamma$ denotes the rate for the intraband scattering of 1s excitons via exciton-phonon interaction and $\gamma$ is the exciton annihilation rate caused by nonradiative Auger decay. **b,** Density of excitons $n_X$ as a function of $t_{PP}$ for a pump fluence $\Phi = 16\mu J/cm^2$. Red spheres: Experimental data. Black line: Rate equation model with $\tau = 150$ fs, $\gamma = 0.13$ cm²/s and $\Gamma = 3.7 \times 10^{12}$ 1/s. **c,** Corresponding data for a pump fluence $\Phi = 42\ \mu J/cm^2$ with the same parameters.

states feature a density $n_{NX}$. Note that excitons within the light cone can also be optically dark, e.g., by virtue of spin selection rules. These states are included in the density $n_{NX}$.

Bright excitons can be directly generated by the pump pulse and subsequently decay either radiatively or by Auger recombination. Alternatively, their density can be reduced by momentum scattering into dark states. Hence $n_{RX}$ fulfills the rate equation:

$$\frac{dn_{RX}}{dt} = G(t) - \frac{1}{\tau}n_{RX} - \frac{1}{2}\gamma(n_{RX} + n_{NX})^2 - \Gamma n_{RX} \qquad (20)$$

where the time-dependent function $G(t)$ considers exciton generation by the pump pulse, $\tau$ is the radiative decay constant, $\gamma$ denotes the Auger decay constant and $\Gamma$ is the momentum scattering rate. The optically dark states, in contrast, are populated via momentum scattering out of the bright states and decay by Auger recombination. The corresponding rate equation reads

$$\frac{dn_{\mathrm{NX}}}{dt} = \Gamma n_{\mathrm{RX}} - \frac{1}{2}\gamma(n_{\mathrm{NX}} + n_{\mathrm{RX}})^2 \tag{21}$$

The total density of 1s excitons $n_X$ measured by the mid-infrared probe is given by

$$n_{\mathrm{X}} = n_{\mathrm{RX}} + n_{\mathrm{NX}} \tag{22}$$

Fitting the experimental data of $n_X$ with a numerical solution of the coupled differential equations one can extract all relevant time constants and rates. Since $\tau = 150$ fs and $\gamma = 0.13$ cm$^2$/s are already known from partially fitting $\Delta E_{max}$ (see Figs. 4a and b in the main text) and the generation rate $G(t)$ is set by the 90-fs pump pulse, adapting the full rate equation model to the experimental data (Supplementary Figs. 8b and c) allows us to extract the exciton-phonon scattering rate $\Gamma = 3.7$ ps$^{-1}$. The temporal evolution of the 1s exciton density $n_X$ is well described for different pump fluences with the same set of parameters.

The momentum scattering rate $\Gamma$ obtained here can be elegantly compared with values of exciton mobilities recently measured in $WSe_2$[18]. Within a ballistic model, the exciton mobility $\mu$ can be written as:

$$\mu = \frac{e}{\Gamma M^*} \tag{24}$$

where $M^*$ is the effective exciton mass. We obtain a mobility $\mu = 700$ cm$^2$/Vs, which is in good agreement with a value found in the literature[18]. The non-radiative bi-molecular decay caused by exciton-exciton annihilation ($\gamma = 0.13$ cm$^2$/s) describes the temporal evolution for longer delay times $t_{PP}$.

With the help of this rate equation model one can estimate the maximum possible quantum yield for resonant injection. This can be done by comparing the time-integrated value of $n_{RX}$ with the density of all injected excitons. Assuming that all bright excitons within the light cone recombine radiatively one can estimate the maximum quantum yield to be 10%. The result, however, should be vastly different for non-resonant excitation far above the fundamental bandgap, where additional loss channels may come into play. For exciton densities lower than in the present case non-radiative decay channels, such as trapping at impurities or surface states of the substrate, will become more important than Auger recombination. This can result in a strongly enhanced PL yield observed for free-standing TMDCs[19]. These extrinsic effects cannot be taken into account in this model.

DOI: 10.1038/NMAT4356

### 12. Pump wavelength dependence of the population decay

Supplementary Figure 9 summarizes the dynamics of the electron-hole pair density of the photoexcited monolayer of $WSe_2$ for various pump wavelengths. All data are taken at room temperature. Non-resonant above-bandgap excitation (pump wavelength: 400 nm; FWHM: 10 nm, Supplementary Fig. 3a) creates unbound electron-hole pairs. The dynamics of the pair density (Supplementary Fig. 9a) is qualitatively different from the temporal traces observed for resonant exciton injection (Figs. 4a and b): It increases rapidly within the time duration of the pump pulse of 90 fs and stays approximately constant within the subsequent time window of 10 ps. Neither the ultrafast 150 fs decay nor the bi-molecular recombination is observed. This is indeed expected since the assignment of the two main features to radiative and Auger recombination, respectively, depends on the presence of excitons.

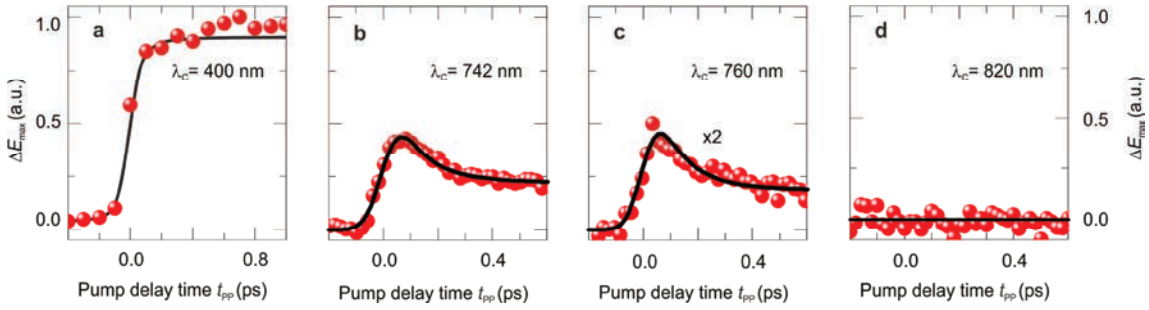


**Supplementary Figure 9 | Population dynamics for various pump wavelengths at $T$ = 295 K.** **a**, Maximum of $\Delta E_{max}$ as a function of $t_{PP}$ (fluence $\Phi = 48\ \mu J/cm^2$) for non-resonant above-bandgap excitation of unbound electron-hole pairs at $\lambda_C = 400$ nm. Red spheres: experiment. Black solid line: guide to the eye. **b,** $\Delta E_{max}(t_{PP})$ for resonant creation of excitons with $\lambda_C = 742$ nm and $\Phi = 16\ \mu J/cm^2$. Red spheres: experiment. Black solid line: rate equation model with $\tau = 150$ fs, $\gamma = 0.13\ cm^2/s$ and $\Gamma = 3.7 \times 10^{12}\ 1/s$. **c,** Analogous data for a pump spectrum centred at $\lambda_C = 760$ nm and $\Phi = 16\ \mu J/cm^2$. Red spheres: experiment. Black solid line: rate equation model with $\tau = 150$ fs, $\gamma = 0.13\ cm^2/s$ and $\Gamma = 2.5 \times 10^{12}\ 1/s$. **d,** For a pump spectrum centred at $\lambda_C = 820$ nm, no measurable mid-infrared response is observed.

The temporal evolution of the exciton density (Supplementary Fig. 9b) performed with a pump spectrum centred at 742 nm, i.e. at the high-energy wing of the interband 1s exciton resonance (Supplementary Fig. 3d), exhibits the fingerprint of excitonic decay discussed in the main paper: An ultrafast exponential decay with a time constant of 150 fs is followed by the bi-molecular dynamics indicative of Auger recombination. The black solid line in Supplementary Fig. 9b shows the rate equation model adapted to the experimental data. The extracted parameters for the rate equation model and the two-dimensional Wannier exciton model are given in the figure caption.

With a slightly longer pump wavelength of 760 nm (Supplementary Fig. 3g), corresponding to excitation at the low-energy wing of the 1s exciton line, the dynamics of the exciton density (Supplementary Fig. 9c) is very similar to the case shown in Supplementary Fig. 9b. Importantly, the same radiative lifetime of $\tau = 150$ fs can be extracted. This finding confirms the microscopic picture of the excitons being responsible for the ultrafast decay (radiative lifetime).

Interestingly, the fraction of excitons decaying within the first 200 fs increases slightly as the pump wavelength is increased from 742 nm (Supplementary Fig. 9b) to 760 nm (Supplementary Fig. 9c). This fact is captured quantitatively by fitting the experimental data via the rate equation model (black solid curves in Supplementary Figs. 9b,c): A reduction of the momentum scattering rate $\Gamma$ by a factor of 1.5 is found as the pump is tuned from 742 nm to 760 nm. This intriguing observation is likely a consequence of an inhomogeneous broadening of the 1s line, where high-energy states may find a larger phase space for scattering.

Finally, exciting the monolayer with a pump centred at 820 nm (Supplementary Fig. 3j) does not lead to any measurable absorption (Supplementary Fig. 9d), since the pump-wavelength is energetically below the 1s excitonic interband resonance of 744 nm.

### 13. Temperature dependence of the exciton dielectric response and dynamics

As an additional test of our microscopic model we investigate the temperature dependence of the ultrafast mid-infrared exciton response. In order to maintain comparable excitation conditions for all temperatures, different interference filters (bandwidth: 10 nm) were used to tune the pump wavelength in resonance with the temperature-dependent 1s excitonic interband transition. The PL spectra and the adapted pump spectra, for three select temperatures, $T = 260$ K, 295 K and 330 K, are shown in Supplementary Figs. 10a-c, respectively, which covers the maximum temperature window accessible to the experimental setup.

Interestingly, the dielectric response functions $\Delta\sigma_1$ and $\Delta\varepsilon_1$ (Supplementary Figs. 10d-i) are qualitatively similar for all temperatures tested. The broad maximum in $\Delta\sigma_1$ and the dispersive shape of $\Delta\varepsilon_1$ are characteristic of the 1s-2p resonance and are well fit by the two-dimensional Wannier exciton model (Supplementary Eq. 14) with parameters given in the figure caption. Briefly, the 1s-2p resonance frequency is independent of temperature. The width of the resonance, in contrast, increases clearly with temperature from $\Delta(260\text{ K}) = 89$ meV via $\Delta(295\text{ K}) = 118$ meV to $\Delta(330\text{ K}) = 126$ meV. This trend suggests phonon scattering to play an important role in the broadening of the 2p state.

DOI: 10.1038/NMAT4356

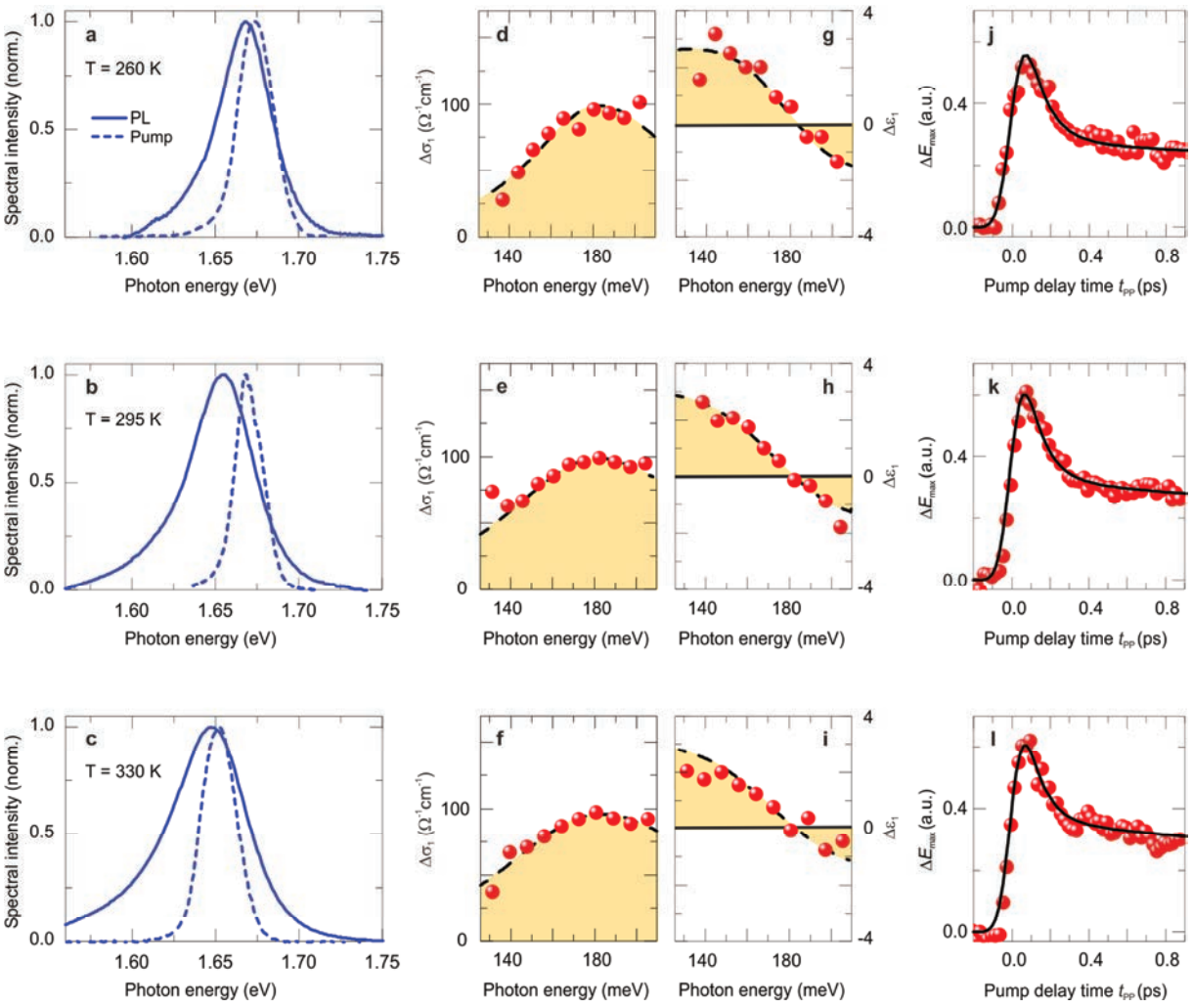


**Supplementary Figure 10 | Mid-infrared response of photoexcited monolayer $WSe_2$ for various lattice temperatures.** **a** – **c**, Measured photoluminescence spectrum of the monolayer (blue solid line) and the pump spectrum (blue dashed line) for three different temperatures (**a**, 260 K, **b**, 295 K, **c**, 330 K). **d** – **f**, Real part of the pump-induced mid-infrared conductivity $\Delta\sigma_1(\hbar\omega)$ of a photoexcited monolayer $WSe_2$ as a function of the photon energy $\hbar\omega$ for three different temperatures (**d**, 260 K, **e**, 295 K, **f**, 330 K), pump fluences $\Phi = 24\ \mu J/cm^2$ and pump delay times $t_{PP}$ = 275 fs. **g** – **i**, Corresponding real part of the dielectric function $\Delta\varepsilon_1(\hbar\omega)$. Red spheres: Experimental data. Black dashed line: **d** – **i**, Two-dimensional Wannier exciton model simultaneously fitting $\Delta\sigma_1$ and $\Delta\varepsilon_1$. The adapted parameters of 1s A exciton density $n_X$, transition energy $E_{res}$, and linewidth $\Delta$, are: **d**, **g**, $n_X = 1.86 \times 10^{12}$ cm$^{-2}$, $E_{res}$ = 183 meV, $\Delta$ = 89 meV. **e**, **h**, $n_X = 2.53 \times 10^{12}$ cm$^{-2}$, $E_{res}$ = 183 meV, $\Delta$ = 118 meV. **f**, **i**, $n_X = 2.62 \times 10^{12}$ cm$^{-2}$, $E_{res}$ = 183 meV, $\Delta$ = 126 meV. **j** – **l** Maximum of the pump induced change $\Delta E_{max}$ as a function of the pump delay time $t_{PP}$ for three different temperatures (**j**, 260 K, **k**, 295 K, **l**, 330 K) and a pump fluence $\Phi = 24\ \mu J/cm^2$. Red spheres: Experimental data. Black solid line: **j** – **l** Rate equation model with $\tau$ = 150 fs, $\gamma$ = 0.13 cm$^2$/s and $\Gamma = 3.1 \times 10^{12}$ 1/s (**j**), $\Gamma = 3.7 \times 10^{12}$ 1/s (**k**), $\Gamma = 4.3 \times 10^{12}$ 1/s (**l**).

Beside the spectral shapes of the response functions, the dynamics of $\Delta E_{max}(t_{pp})$, which is proportional to the 1s exciton density, confirms the microscopic picture given in the main paper. The density dynamics is displayed in Supplementary Figs. 10j-l for the three selected temperatures. In all cases, an ultrafast initial decay of a subset of excitons is observed, followed by a slower bi-molecular dynamics. Importantly, the time constant of the ultrafast decay remains temperature independent – as expected for radiative recombination of excitons located within the light cone. Interestingly, however, the relative weight of the fast and the slower decay dynamics exhibits a clear trend: With increasing temperature, the share of excitons undergoing ultrafast radiative recombination decreases monotonically. This observation is quantitatively captured by adapting the rate equation model to the experimental data. Best agreement is obtained with the same fast decay constant of $\tau = 150$ fs, for all temperatures. However, the momentum scattering rate increases from $\Gamma = 3.1 \times 10^{12}$ 1/s to $\Gamma = 4.3 \times 10^{12}$ 1/s as the temperature is raised from $T = 260$ K to 330 K. This fact underpins the role of phonons for momentum scattering of excitons described by the rate $\Gamma$.


1. Haug, H., Koch, S. W. *Quantum Theory of the Optical and Electronic Properties of Semiconductors* (World Scientific, 2009).
2. Kumar, A. & Ahluwalia, P. K. Tunable dielectric response of transition metal dichalcogenides $MX_2$ (M=Mo, W; X=S, Se, Te): Effect of quantum confinement. *Physica B* **407,** 4627-4634 (2012).
3. Yang, X. L., Guo, S. H., Chan, F. T., Wong, K. W. & Ching, W. Y. Analytic solution of a two-dimensional hydrogen atom. I. Nonrelativistic theory. *Phys. Rev. A* **43,** 1186 (1991).
4. Berkelbach, T. C., Hybertsen, M. S. & Reichman, D. R. Theory of neutral and charged excitons in monolayer transition metal dichalcogenides. *Phys. Rev. B* **88,** 045318 (2013).
5. Chernikov, A., Berkelbach, T. C., Hill, H. M., Rigosi, A., Li, Y., Aslan, O. B., Reichman, D. R., Hybertsen, M. S. & Heinz, T. F. Exciton Binding Energy and Nonhydrogenic Rydberg Series in Monolayer $WS_2$. *Phys. Rev. Lett.* **113,** 076802 (2014).
6. Zhang, C., Wang, H., Chan, W., Manolatou, C. & Rana, F. Absorption of light by excitons and trions in monolayers of metal dichalcogenide $MoS_2$: Experiments and theory. *Phys. Rev. B* **89,** 205436 (2014).
7. Kaindl, R. A., Hägele, D., Carnahan, M. A. & Chemla, D. S. Transient terahertz spectroscopy of excitons and unbound carriers in quasi-two-dimensional electron-hole gases. *Phys. Rev. B* **79,** 045320 (2009).
8. He, K., Kumar, N., Zhao, L., Wang, Z., Mak, K. F., Zhao, H. & Shan, J. Tightly Bound Excitons in Monolayer $WSe_2$. *Phys. Rev. Lett.* **113,** 026803 (2014).

9. Wang, G., Marie, X., Gerber, I., Amand, T., Lagarde, D., Bouet, L., Vidal, M., Balocchi, A. & Urbaszek, B. Gaint enhancement of the optical second-harmonic emission of $WSe_2$ monolayers by laser excitation at exciton resonances. *Phys. Rev. Lett.* **114,** 097403 (2015).
10. Jones, A. M., Yu, H., Ghimire, N. J., Wu, S., Aivazian, G., Ross, J. S., Zhao, B., Yan, J., Mandrus, D. G., Xiao, D., Yao, W. & Xu, X. Optical generation of excitonic valley coherence in monolayer $WSe_2$. *Nature Nanotech.* **8,** 634-638 (2013).
11. Wang, D., Bouet, L., Lagarde, D., Vidal, M., Balocchi, A., Amand, T., Marie, X. & Urbaszek, B. Valley dynamics probed through charged and neutral exciton emission in monolayer $WSe_2$. *Phys. Rev. B* **90,** 075413 (2014).
12. Srivastava, A., Sidler, M., Allain, A. V., Lembke, D.S., Kis, A. & Imamoglu A. Valley Zeemann effect in elementary optical excitations of monolayer $WSe_2$. *Nature Phys.* **11,** 141 (2015).
13. Fang, H., Tosun, M., Seol, G., Chang, T. C., Takei, K., Guo, J. & Javey, A. Degenerate n-doping of few-layer transition metal dichalcogenides by Potassium *Nano Lett.* **13,** 1991 (2013).
14. Kumar, N., Cui, Q., Ceballos, F., He, D., Wang, Y. & Zhao, H. Exciton-exciton annihilation in $MoSe_2$ monolayers. *Phys. Rev. B* **89,** 125427 (2014).
15. Huber, R., Tauser, T., Brodschelm, A., Bichler, M., Abstreiter, G. & Leitenstorfer, A. How many-particle interactions develop after ultrafast excitation of an electron-hole plasma. *Nature* **414,** 286 (2001).
16. Kim, K. W., Pashkin, A., Schäfer, H., Beyer, M., Porer, M., Wolf, T., Bernhard, C., Demsar, J., Huber, R. & Leitenstorfer, A. Ultrafast transient generation of spin-density-wave order in the normal state of $BaFe_2As_2$ driven by coherent lattice vibrations. *Nature Mater.* **11,** 497 (2012).
17. Porer, M., Leierseder U., Ménard, J.-M., Dachraoui, H., Mouchliadis, L., Perakis, I. E., Heinzmann, U., Demsar, J., Rossnagel, K. & Huber, R. Non-thermal separation of electronic and structural orders in a persisting charge density wave. *Nature Mater.* **13,** 857-861 (2014).
18. Cui, Q., Ceballos, F., Kumar, N. & Zhao, H. Transient Absorption Microscopy of Monolayer and Bulk $WSe_2$. *ACS Nano* **8,** 2970-2976 (2014).
19. Mak, K. F., Lee, C., Hone, J., Shan, J & Heinz, T. F. Atomically thin $MoS_2$: A new direct-gap semiconductor. *Phys. Rev. Lett.* **105,** 136805 (2010).